Polymer 50 (2009) 2906–2918

Contents lists available at ScienceDirect

Polymer

journal homepage: www.elsevier.com/locate/polymer

Molecular miscibility and chain dynamics in POSS/polystyrene blends: Control of POSS preferential dispersion states

Rahul Misra, Alp H. Alidedeoglu, William L. Jarrett, Sarah E. Morgan*

School of Polymers and High Performance Materials, University of Southern Mississippi, 118 College Dr., Box 10076, Hattiesburg, MS 39406-0076, USA

ARTICLE INFO

Article history:
Received 9 December 2008
Received in revised form
19 March 2009
Accepted 20 March 2009
Available online 16 April 2009

Keywords:
Polyhedral oligomeric silsesquioxane (POSS)
Dispersion
Chain dynamics

ABSTRACT

Polyhedral oligomeric silsesquioxane (POSS)/polystyrene nanocomposites with two different POSS molecules, octaisobutyl POSS (Oib-POSS) and trisilanolphenyl POSS (Tsp-POSS), were prepared *via* solution blending in toluene. Solution dynamics analysis indicates random coil conformation of neat PS and POSS/PS blends. Morphology analysis (AFM/TEM) revealed differences in the preferential dispersion states of Tsp- and Oib-POSS molecules. Tsp-POSS, with its greater predicted solubility in PS, exhibited nanoscale dispersion throughout the bulk leading to transparent films. In contrast, Oib-POSS, with its reduced predicted solubility in PS, exhibited preferential surface segregation, aggregation of POSS particles and hazy films. Estimated fractional surface coverage for the materials, based on surface energy measurements, indicated 15% coverage by Tsp-POSS and 78% for Oib-POSS. Solid-state NMR relaxation studies suggest aggregation of Oib-POSS molecules. Additional NMR studies, including silicon CP/MAS, 2D HETCOR, and WISE, indicate close spatial proximity and interaction of Tsp-POSS molecules with PS chains, contrasting with poor interaction and immiscibility of Oib-POSS with PS.

1. Introduction

A major challenge in the development of high performance polymeric nanocomposites is the control of nanoparticle dispersion. Polyhedral oligomeric silsesquioxane (POSS) nanostructured chemicals, with their hybrid organic–inorganic nature and flexible functionalization with a variety of organic substituents, yield possibilities to control dispersion and tune compatibility in a wide range of polymer systems [1,2]. POSS molecules are cage-like structures described by the general chemical structure $R(SiO_{1.5})_n$, where $n = 8$, 10 or 12. This cage is surrounded by a corona of organic groups and it may be a fully condensed "closed" or an "open" structure. Depending on the nature of the substituents, the size of POSS nanoparticles ranges from 1 to 3 nm [3]. POSS molecules can be incorporated into a polymer matrix by co-polymerization or physical blending routes. The majority of the studies reported to date have focused on the synthesis of POSS copolymers [4–11]. Limited studies have appeared on the dispersion and bulk thermomechanical characteristics of physically blended POSS/polymer films prepared *via* melt [12–14] and solution [15,16] blending. Although bulk solution characteristics such as viscosity [17] have been reported recently, detailed understanding of chain dynamics and conformations in POSS/polymer nanocomposite solutions and films, critical for predicting segregation and dispersion behavior, is not currently available.

Surface segregation is defined as the preferential enrichment of one component of a multi-component system at the air–surface interface. The concept of self-stratification was introduced in 1976 by Funke et al. [18] and is well documented for polymer blends [19,20], block copolymers [21,22] and polymer solutions [23]. Surface segregation in POSS/polymer blends has been reported from our laboratories and by other researchers [24–29]. We demonstrated that surface segregation of selected POSS nanoparticles leads to improved surface hydrophobicity and tribomechanical characteristics of melt blended POSS/polymer nanocomposites [24,25]. Takahara and coworkers [26] reported a strong influence of POSS nanofillers on the surface dewetting characteristics of POSS-filled thin polystyrene films. Similarly, Esker and coworkers [27,28] studied the phase separation behavior and morphological evolution in dewetting thin films of POSS/poly(*tert*-butyl acrylate) blends as a function of annealing temperature and time. Fukuda et al. [29] reported a higher concentration of POSS on the film surface for PMMA/POSS blends, resulting in increased hydrophobicity. In other nanocomposite studies, Gupta et al. [30] reported the entropy driven segregation of surface modified cadmium selenide/zinc sulfide core-shell nanoparticles in multilayer composite structures. Similarly, Mackey and coworkers [31,32] investigated the self-assembly and miscibility behavior of cross-linked polystyrene nanoparticles and dendritic polyethylene

* Corresponding author. Tel.: +1 601 266 5296; fax: +1 601 266 5635.
E-mail address: sarah.morgan@usm.edu (S.E. Morgan).

0032-3861/$ – see front matter © 2009 Elsevier Ltd. All rights reserved.
doi:10.1016/j.polymer.2009.03.057

blended with high molecular weight polystyrene. The ratio of the radius of gyration (R_g) of polymer chains to nanoparticle radius was found to be an important factor in determining compatibility, diffusion, and the segregation process.

Solid-state nuclear magnetic resonance (NMR) spectroscopy has emerged as a valuable tool to probe the molecular miscibility, interactions and chain dynamics in multi-component hybrid polymer systems [33–35]. Recently, Strachota et al. [36] utilized solid-state NMR to study the domain selective relaxation behavior in a variety of POSS reinforced epoxy networks and reported marked motional heterogeneities.

The current study is an attempt to understand the ability to control and tailor the dispersion states of POSS in polymeric films prepared from solution. The effects of POSS structure, molecular miscibility, and chain dynamics on the dispersion and segregation behavior of POSS nanoparticles in solution blended POSS/polystyrene (PS) nanocomposites are examined. Two POSS molecules, a closed cage octaisobutyl POSS (Oib-POSS) and an open cage trisilanolphenyl POSS (Tsp-POSS), with differing solubility parameters in relation to that of PS, were chosen for evaluation. Solution dynamics were probed *via* static and dynamic light scattering. Molecular miscibility, chain dynamics and dispersion properties in films were investigated utilizing multiple solid-state NMR techniques, including ^{13}C CP/MAS, 2D ^{1}H–^{13}C and ^{1}H–^{29}Si HETCOR, and wide-line separation (WISE) spectroscopy, as well as AFM, TEM and contact angle studies.

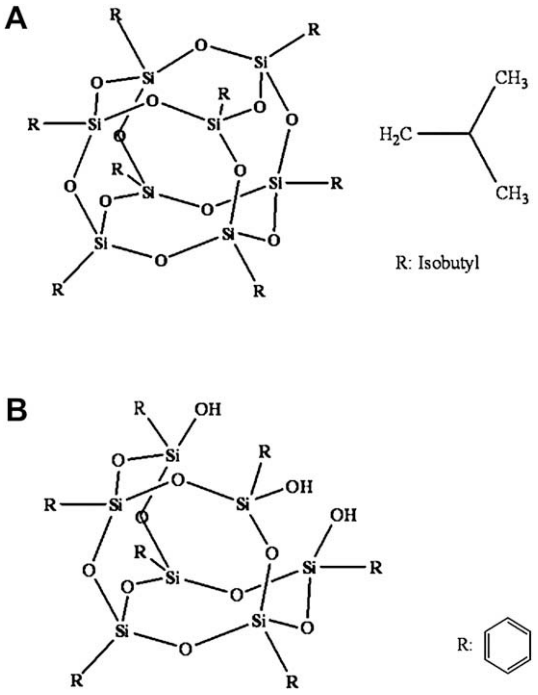

Fig. 1. Molecular structure of (A) Octaisobutyl POSS (B) Trisilanolphenyl POSS.

2. Experimental

2.1. Materials

Polystyrene (M_w 280,000 Da) and HPLC grade toluene were purchased from Sigma–Aldrich Company (St. Louis, MO). A closed cage octaisobutyl POSS (MSO825) (Oib-POSS) and an open cage trisilanolphenyl POSS (SO1458) (Tsp-POSS) were provided by Hybrid Plastics Inc. (Hattiesburg, MS) as crystalline white powders. All materials were used as received unless otherwise specified. The chemical structures of Oib-POSS and Tsp-POSS are shown in Fig. 1(A) and (B) respectively. Supplier analysis confirms that these are pure cages with no oligomers present.

2.2. Composite preparation

POSS/PS hybrid polymer composites (HPCs) were prepared at concentrations of 0, 5, and 10 wt.% of POSS in PS. Both POSS and PS were solution blended in toluene by stirring blend solutions (concentration 10 wt.%) for 12 h. Films were prepared using a draw-down bar on a clean glass slide. The films were dried at room temperature for 2 days followed by additional drying under vacuum at 110 °C (above the glass transition temperature of PS) for another 12 h to remove any residual solvent.

2.3. Refractive index measurements

Refractive index of neat PS and HPC solutions was measured using a Bausch & Lomb Abbe-3L refractometer. The prism surface was covered uniformly by placing 2–3 drops of sample using a glass pipette. To avoid scratching of the prism surface, the tip of glass pipette should not touch the prism while placing the sample. Refractive index was measured by placing a crisp demarcation line between the dark and the bright region at the center of the cross-hair. In addition, the prism surface was gently cleaned using ethanol and a soft tissue paper after each measurement.

2.4. Multiangle laser-light scattering (MALLS)

Multiangle laser-light scattering experiments were performed using a DAWN-DSP (Wyatt Technology Corp., Santa Barbara, CA) in batch mode at 27 °C. Vertically polarized He–Ne laser light ($\lambda = 690$ nm) was utilized as an incident beam. Scintillation vials were cleaned thoroughly with filtered DI water and dried before use. POSS/PS blend solutions with concentrations ranging from 1 to 5 mg/ml were prepared using filtered HPLC grade toluene (Sigma–Aldrich). Blend solutions were filtered using 0.45 μm PTFE filters. The refractive index increment (dn/dc) for each blend solution was measured using a Bausch & Lomb Abbe-3L refractometer. Baseline was established with filtered toluene. Detectors were normalized using a polystyrene standard ($M_w = 44{,}000$ gm/mol) solution. Samples were analyzed in batch mode for 5 min. Radius of gyration (R_g), molecular weight (M_w), and second virial coefficient (A_2) were obtained by analyzing Zimm plots using ASTRA for Windows software (version 4.90.07).

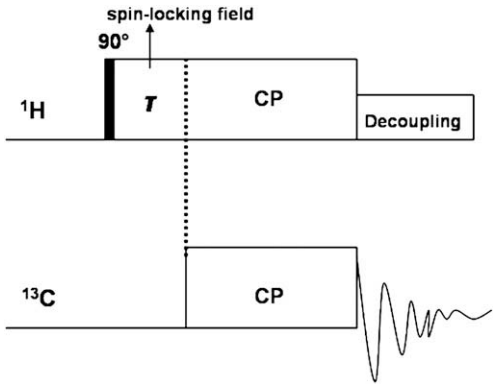

Fig. 2. Schematic representation of $T_{1\rho}(H)$ relaxation experiment pulse sequence.

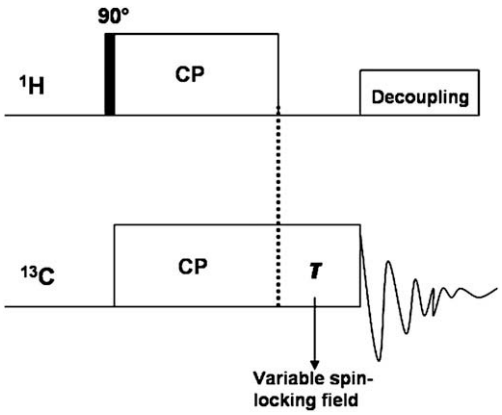

Fig. 3. Schematic representation of $T_{1\rho}$(C) relaxation experiment pulse sequence.

2.5. Dynamic light scattering (DLS)

Dynamic light scattering studies were conducted to evaluate the aggregation behavior of POSS nanoparticles in blend solutions by measuring hydrodynamic radius (R_h). DLS measurements were performed using a Malvern Zetasizer Nanoseries (Worcestershire, UK) with a 4 mW He–Ne laser operating at $\lambda = 632.8$ nm, an avalanche photodiode detector with high quantum efficiency, and an ALV/LSE-5003 multiple tau digital correlator electronics system.

2.6. Atomic force microscopy (AFM) surface morphology

Surface morphology studies were conducted on a MultiMode™ scanning probe microscope from Veeco Instruments, Inc. (Santa Barbara, CA). A silicon probe with a 125 μm long silicon cantilever, nominal force constant of 40 N/m, and resonance frequency of 275 kHz was used for tapping mode surface topography studies. Surface topographies of film samples were studied on 1 μm × 1 μm scan size areas at an image resolution of 512 × 512 pixels and a scan rate of 1 Hz. Multiple areas were imaged and figures show representative morphology.

2.7. Transmission electron microscopy – energy dispersive X-ray (TEM-EDAX) bulk morphology

An ultra-high-resolution transmission electron microscope (JOEL-2100, Joel Ltd., Tokyo, Japan), at an accelerating voltage of 200 kV, was utilized to investigate the dispersion of POSS as well as the resulting microstructure of POSS/PS HPCs. TEM samples were prepared by putting a drop of diluted HPC solution on a 600 mesh copper grid and allowing the solvent to evaporate. Elemental analysis of these samples was acquired using energy dispersive X-ray in conjunction with TEM using EDAX Genesis software.

2.8. Wide angle X-ray diffraction (WAXD)

X-ray diffraction studies of POSS/PS HPCs were conducted on the film samples, and neat POSS samples were tested in powder form. Diffraction patterns were obtained using a Rigaku D/MAX-Ultima-III Diffractometer in transmission mode at room temperature using Cu Kα radiation at a tube current of 44 mA and an acceleration voltage of 40 kV. Scan range was 3°–35° at a step interval of 0.01° and a scanning rate of 2°/min.

2.9. Surface energy measurements

Surface energy of neat POSS powders was measured according to the Washburn method [37] utilizing two probe liquids – benzyl alcohol and diiodomethane (CH_2I_2). The packed cell method was used on a Kruss K100 Tensiometer. The cell, a standard Kruss FL12 cell, was packed with 0.50 gm of powder for each experiment. Hexane was used as the perfect wetting liquid for the material constant experiments. Additionally, the surface energy of HPC film surfaces was calculated utilizing the Fowkes [38] and Owens–Wendt method [39] by measuring the contact angles with deionized water and glycerol. Static contact angles were measured using the sessile drop technique by a Ramè–Hart goniometer coupled with DROPimage® data analysis software.

2.10. Solid-state ^{13}C cross-polarization/magic angle spinning NMR spectroscopy

Solid-state NMR spectra were obtained utilizing a Varian UNITY INOVA 400 NMR spectrometer (Varian Inc., Palo Alto, CA) equipped with a standard Chemagnetics 7.5 mm PENCIL™ style probe. Samples were placed into zirconia rotor sleeves, sealed with Teflon™ caps, and spun at a rate of 4.0 kHz. Carbon spectra were obtained using the standard cross-polarization/magic angle spinning (CP/MAS) technique. High-power proton decoupling was applied during data acquisition to remove ^{1}H–^{13}C dipolar coupling and yield high-resolution spectra [40]. Additionally, Total Suppression of Spinning Side bands (TOSS) technique was implemented to remove spinning side bands [41]. The ^{1}H 90° pulse width was 4.0 μs, and the cross-polarization contact time was 1 ms. The dead time delay was 6.4 μs between cross-polarization and proton dipolar coupling. The data acquisition time was 45 ms, with a recycle delay of 7.5 s between scans.

Proton rotating-frame spin-lattice relaxation ($T_{1\rho}$) experiments were performed using a Chemagnetics 4.0 mm or 7.5 mm probes. Spectra were acquired by applying a ^{1}H RF spin-locking field prior to cross-polarization. Fig. 2 shows the $T_{1\rho}$ (H) pulse sequence; For the 4.0 mm probe the ^{1}H 90° pulse width was 3.5 μs, the cross-polarization contact time was 500 μs, and the dead time delay was 6.4 μs. The data acquisition period was 30 ms, with a ^{1}H decoupling field of 71.4 kHz applied to remove ^{1}H–^{13}C dipolar coupling. The spin rate was 6 kHz, and the recycle delay between scans was 7 s. Spectra acquired using the 7.5 mm probe used a ^{1}H 90° pulse width of 5.5 μs, a cross-polarization contact time of 500 μs, and a dead time delay of 6.4 μs, a data acquisition period of 30 ms, a spinning rate of 4 kHz, and a ^{1}H decoupling field of 67.6 kHz. The strength of the spin-locking field was approximately the same for both probes (~70 kHz). Carbon rotating-frame spin-lattice relaxation ($T_{1\rho}$ (C)) experiments (Fig. 3) were performed using the 7.5 mm CP/MAS probe. Spectra were obtained by

Table 1
Theoretical solubility parameter values for PS, Oib-POSS, and Tsp-POSS.

Sample	ρ (gm/cm^3)	M_o (gm/mol)	ΣG_i (kcal cm^3/mol)$^{1/2}$	δ (cal/cm^3)$^{1/2}$
PS	1.00	104	0.90	9.2
Oib-POSS	0.92	872	7.43	7.8
Tsp-POSS	1.16	930	7.93	9.8

Table 2
Refractive index of PS and POSS/PS HPC solutions.

Sample	RI
PS	1.5083
Tsp-POSS/PS	1.5054
Oib-POSS/PS	1.5041

Table 3
Dynamic and static light scattering data for PS and POSS/PS solutions (± values indicate one standard deviation).

Sample	R_h (nm)	R_g (nm)	$x = (R_g/R_h)$	$M_w \times e^{-5}$ (gm/mol)	$A_2 \times e^{-5}$ (mol ml/gm^2)
PS	19.8 ± 1.1	27.0 ± 2.0	1.36 ± 0.2	2.8 ± 0.1	5.1 ± 0.2
Tsp-POSS/PS	16.8 ± 1.5	23.5 ± 6.5	1.39 ± 1.1	2.9 ± 0.2	5.8 ± 0.5
Oib-POSS/PS	22.5 ± 2.1	33.0 ± 7.5	1.47 ± 2.2	2.9 ± 0.5	8.2 ± 0.7

applying a ^{13}C RF spin-locking field immediately after the cross-polarization pulse. The length of spin-locking pulse was varied from 0.25 to 10 ms, and RF-fields of 42.8, 45.5, 50, 55.6, and 63.6 kHz were used.

2.11. Solid-state ^{29}Si NMR spectroscopy

Solid-state ^{29}Si NMR spectra were obtained using a 7.5 mm Chemagnetics standard CP/MAS probe. The standard CP/MAS technique with high-power proton decoupling applied during data acquisition was used [40]. For ^{29}Si spectra, the ^{1}H 90° pulse width was 4.0 μs, the cross-polarization contact time was 5 ms, and the dead time delay was 6.4 μs. The data acquisition time was 45 ms, with a recycle delay of 4.5 s utilized between consecutive scans. Approximately 1500 scans were accumulated per spectrum. For each spectrum, the free induction decay (FID) was zero-filled to 32k points and a Gaussian filter was applied prior to Fourier transformation.

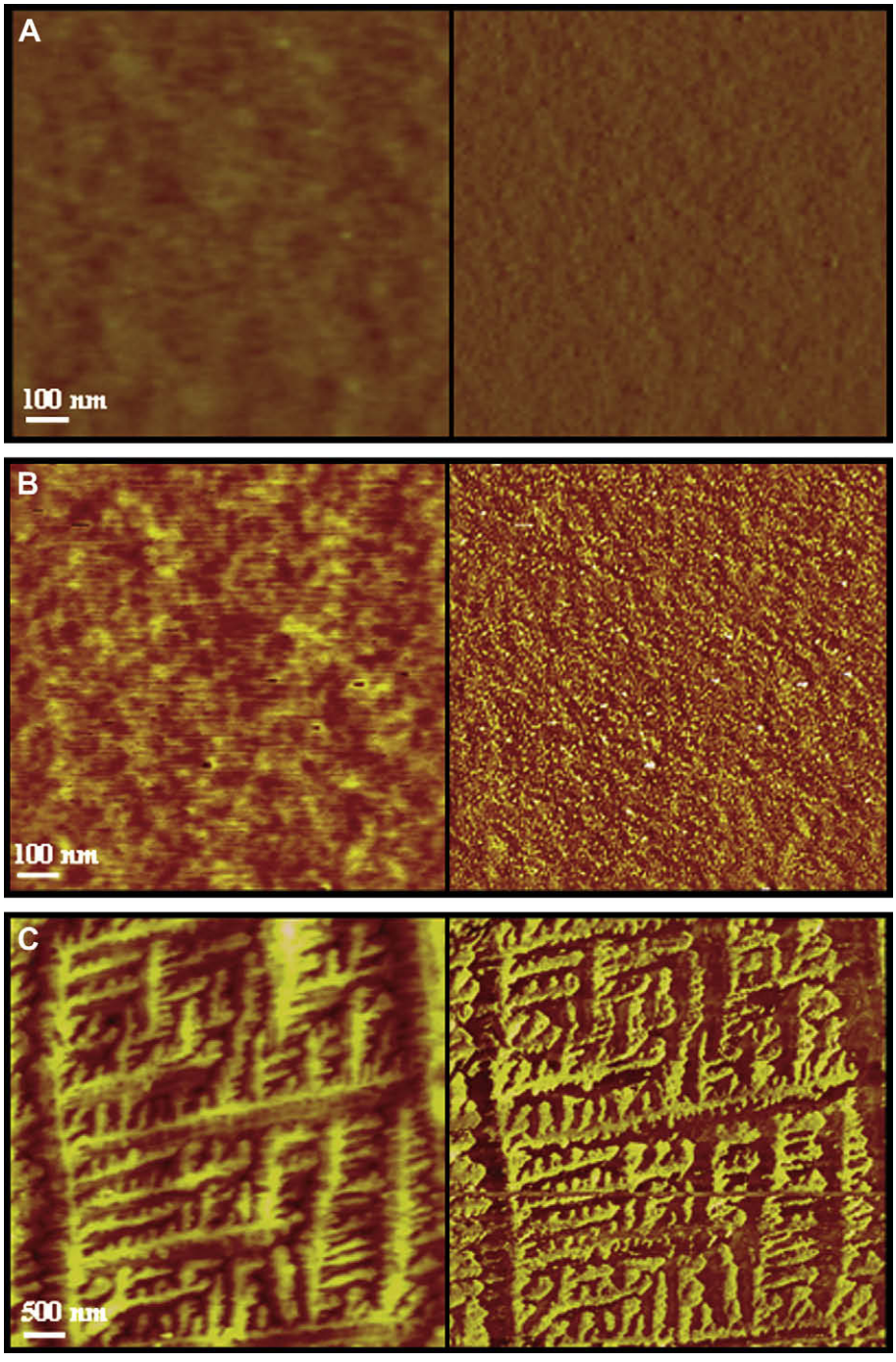

Fig. 4. AFM height (left) and phase (right) images of (A) Neat PS (B) Tsp-POSS/PS (C) Oib-POSS/PS HPCs.

Table 4
AFM particle size analysis of POSS/PS HPCs.

Dimension	Mean	Minimum	Maximum	Sigma
Tsp-POSS/PS				
Diameter (nm)	5.7	2.2	38.9	5.1
Length (nm)	12.4	2.8	87.9	14.8
Oib-POSS/PS				
Diameter (nm)	48.9	11.0	436	67.8
Length (nm)	81.8	13.8	851	128

Table 5
AFM surface roughness of PS and POSS/PS HPCs.

Sample	RMS roughness (nm)	Mean roughness (nm)	Max. height (nm)
PS	0.17	0.13	1.8
Tsp-POSS/PS	0.19	0.16	2.3
Oib-POSS/PS	4.64	3.88	24.5

2.12. Solid-state ^{1}H–^{13}C and ^{1}H–^{29}Si HETCOR 2D NMR spectroscopy

Solid-state ^{1}H–^{13}C HETCOR spectra were obtained using sample spinning rate of 3.0 kHz. Homonuclear proton decoupling during t_1 evolution was achieved *via* frequency-switched Lee–Goldburg (FSLG) method [42]. The number of scans accumulated for each t_1 point was 192 with t_1 phase cycling achieved using the time proportional phase incrementation (TPPI) method. Selective ^{1}H–^{13}C and t_2 acquisition times were 500 μs and 20 ms, respectively. In addition, the TOSS pulse sequence was utilized to suppress the side bands in the F_2 dimension [41]. ^{1}H–^{29}Si HETCOR spectra were obtained using a spin rate of 2.5 kHz with a cross-polarization and t_2 acquisition time of 1 ms and 20 ms, respectively. The number of scans accumulated for each t_1 point using TPPI phase cycling was 128 with a 4.5 s recycle delay between them. Both dimensions were zero-filled to 2k points and a forward linear prediction was applied to t_1 prior to 2D Fourier transformation. For the ^{1}H dimension the scale factor was adjusted such that the shift difference between the aliphatic and aromatic protons was ~6 ppm. Data processing was performed using Varian 6.1C software.

2.13. Wide-line separation (WISE) NMR spectroscopy

Solid-state wide-line separation (WISE) NMR spectroscopy was performed using a standard Chemagnetics 7.5 mm PENCIL™ style probe and sample spinning rate of 3.0 kHz [43,44]. Side bands due to the aromatic ring carbons were suppressed using TOSS. The ^{1}H 90° pulse width was 4.0 μs, the cross-polarization contact time was 500 μs, and the dead time delay was 6.4 μs. The data acquisition time was 45 ms, with a recycle delay of 4 s utilized between the scans. Sweep widths in ^{1}H and ^{13}C spectra were 1250 and 301 ppm,

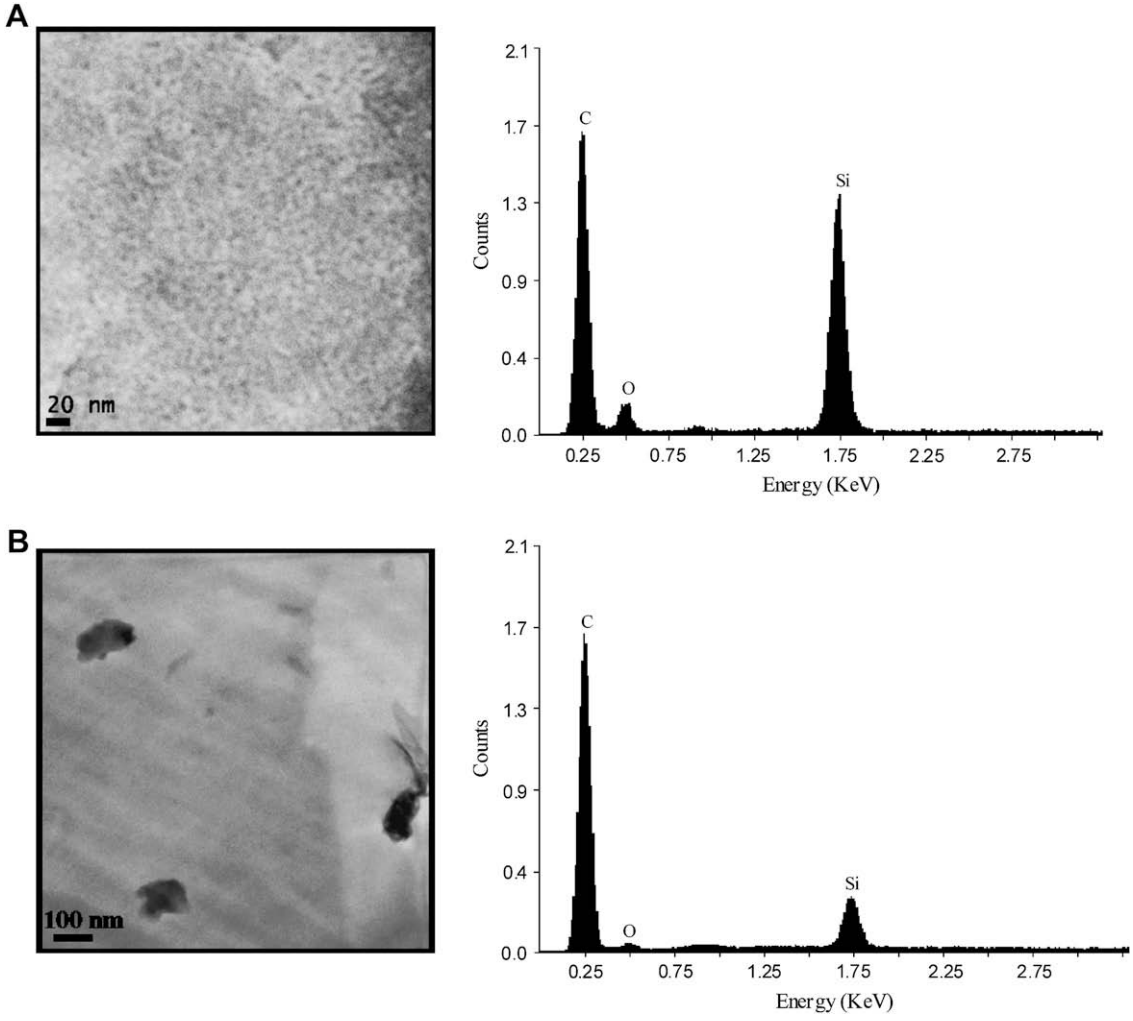

Fig. 5. TEM micrographs and corresponding EDAX elemental analysis of (A) Tsp-POSS/PS (B) Oib-POSS/PS HPCs.

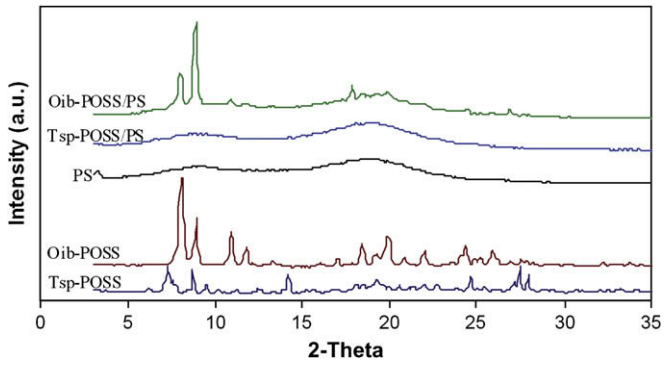

Fig. 6. Wide angle X-ray diffractograms of POSS/PS HPCs.

Table 6
Surface energy of neat PS, POSS, and POSS/PS HPCs.

Sample	Surface energy (mN/m)
Neat PS	34.0
Neat Oib-POSS	21.3
Neat Tsp-POSS	23.7
Tsp-POSS/PS	35.0
Oib-POSS/PS	24.0

respectively. The number of t_1 increments was 128 with 128 scans per increment. TPPI phase cycling was used to obtain phase-sensitive data, with an additional 192 points added to the F_1 dimension *via* linear prediction. Both dimensions were zero-filled to 2048 points with Lorentzian and Gaussian apodization applied to t_1 and t_2 prior to Fourier transformation.

3. Results and discussion

To understand and predict the compatibility and dispersion characteristics of POSS molecules in a PS matrix, theoretical solubility parameters (δ) were estimated *via* Hoy's method [45,46]. Materials with similar solubility parameters exhibit greater compatibility and better dispersion characteristics than those with widely differing solubility parameters. In recent studies of POSS/nylon [25] and POSS/polysiloxane [47] melt blends, good agreement between the theoretical solubility parameters and observed microscopic dispersion of POSS particles was reported. Solubility parameters and group molar-attraction constants (ΣG_i) values for the materials used in this study are shown in Table 1. As expected

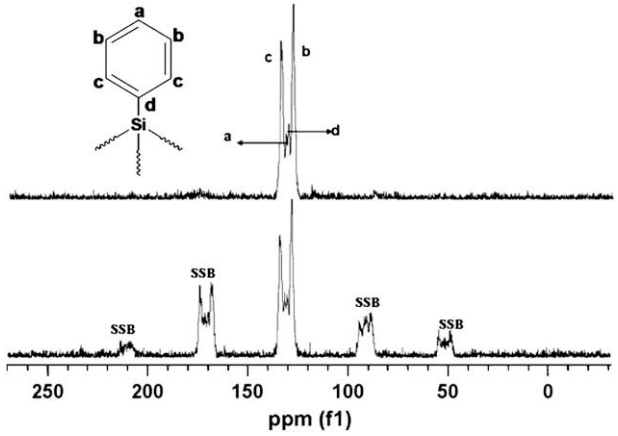

Fig. 7. ^{13}C CP/MAS spectra of Tsp-POSS (A) before and (B) after TOSS sequence.

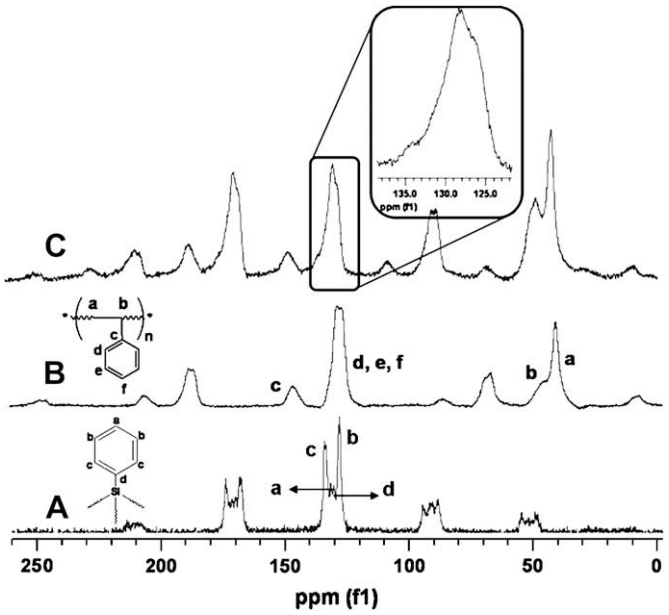

Fig. 8. ^{13}C CP/MAS spectra of (A) neat Tsp-POSS (B) neat PS (C) Tsp-POSS/PS HPC.

based on the chemical structures, calculated solubility parameter for Tsp-POSS is closer to that of PS (difference in solubility parameter $\Delta\delta_{\text{Tsp-POSS/PS}} = 0.6\,(\text{cal/cm}^3)^{1/2}$), than δ for Oib-POSS ($\Delta\delta_{\text{Oib-POSS/PS}} = 1.4\,(\text{cal/cm}^3)^{1/2}$). Thus better compatibility and dispersion characteristics are expected for Tsp-POSS in PS.

Refractive index values of neat PS and POSS/PS HPC solutions are shown in Table 2. At 10 wt.% POSS concentration, all solutions exhibit optical transparency with virtually no change in the refractive index, indicating the solubility of POSS molecules and PS chains at the concentrations evaluated. Films formed from Tsp-POSS/PS solutions were transparent, but the Oib-POSS/PS films were hazy, attributed to aggregation and segregation of the Oib-POSS molecules.

Multiangle laser-light scattering and dynamic light scattering studies were performed to study PS/POSS interactions in solution. Table 3 shows the hydrodynamic radius (R_h), radius of gyration (R_g), average molecular weight (M_w), and second virial coefficient (A_2) for neat polymer and POSS blends in toluene. The A_2 value and R_g/R_h ratio determined for PS agree with literature reports for PS in

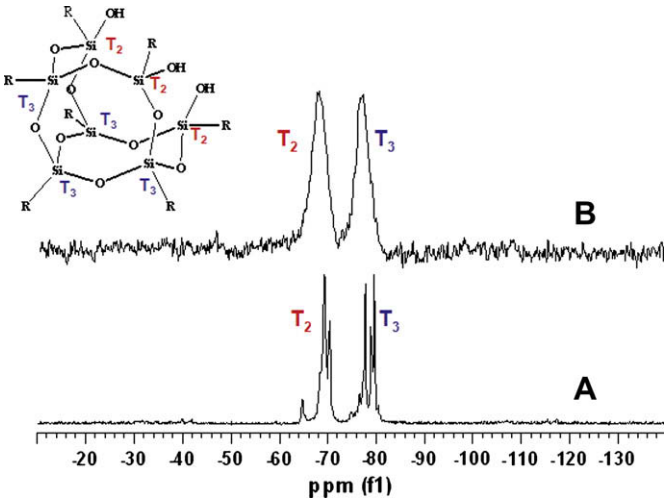

Fig. 9. ^{29}Si spectra of (A) Tsp-POSS (B) Tsp-POSS/PS samples.

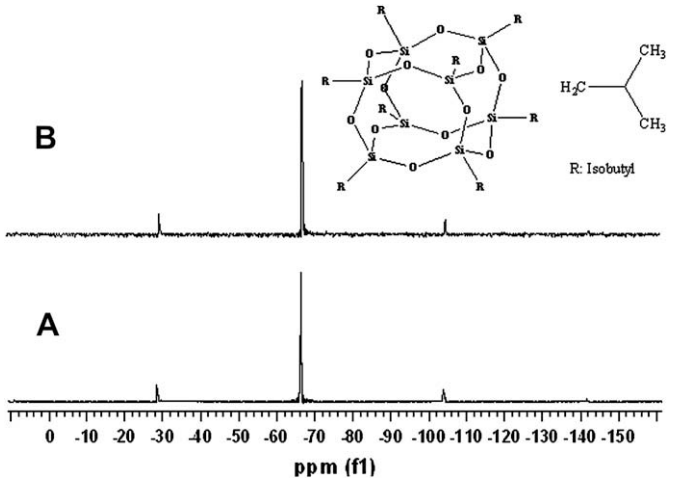

Fig. 10. ^{29}Si spectra of (A) Oib-POSS (B) Oib-POSS/PS samples.

toluene [48] and the measured molecular weight matches the supplier reported value. In general, measured values for the PS–POSS blends show greater variability than the PS homopolymer parameters, indicating that there may be associations of varying sizes in the POSS/PS solutions. These aggregates act as an independent scattering source and influence intra- and inter-particle interference of light waves, contributing to higher variability. In addition to aggregation, factors including solution concentration, nature of solvent, mixed solvent systems, and aggregate distribution have also been reported to contribute to variability in light scattering experiments [49–51]. In our studies, average values determined for A_2, R_h and R_g are higher for Oib-POSS/PS blends than those measured for neat PS, indicating more expanded PS chains in the presence of Oib-POSS. The Tsp-POSS/PS blends, on the other hand, exhibit values within one standard deviation of those measured for neat PS. These differences can be explained by the difference in solubility parameters. Tsp-POSS is predicted to show greater interaction with the PS chain, and thus a smaller radius is expected. Oib-POSS, on the other hand, owing to its larger difference in solubility parameter and structural incompatibility with PS acts as a defect in the PS chain conformation. This increases the mass weighted average distance from the center of mass and results in a higher radius value. Calculated R_g/R_h ratios indicate that all three solutions exhibit random coil conformation in toluene solution, as they fall in the range of values generally considered to represent random coils (R_g/R_h of 1.27–2.05) [52,53].

Tapping mode AFM height and phase images of the samples are shown in Fig. 4 (A)–(C). Neat PS exhibits a smooth featureless surface (root mean square roughness, RMS, of 0.17 nm), while the POSS samples show raised features attributed to POSS aggregates and crystallites. Oib-POSS/PS samples exhibit relatively large raised and elongated surface features (avg. diameter ~50 nm) with broad particle size distribution, while Tsp-POSS/PS samples exhibit surface features an order of magnitude smaller in size (avg. diameter ~5 nm) with narrow size distribution (Table 4). Oib-POSS samples exhibit significantly higher roughness values (RMS roughness = 4.6 nm), while Tsp-POSS blends yield roughness values similar to those of the neat PS surface (RMS roughness = 0.19 nm) (Table 5). Surface morphology analysis indicates preferential segregation of Oib-POSS aggregates to the surface, which is further

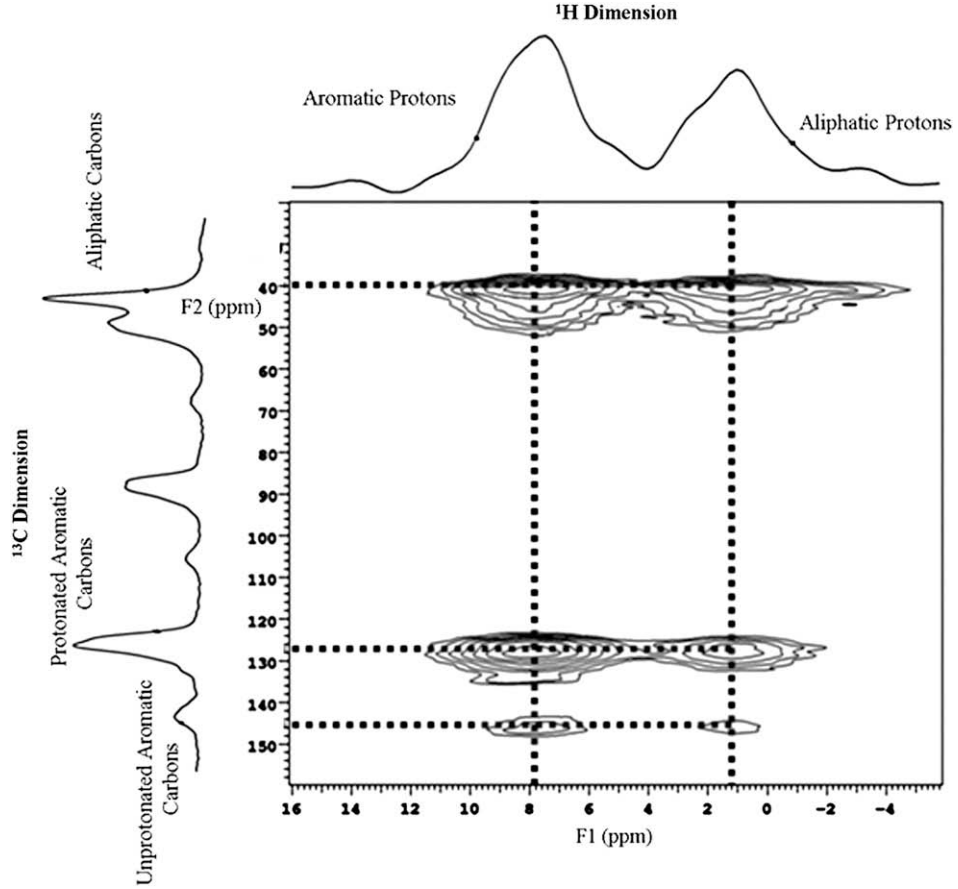

Fig. 11. ^{13}C{^{1}H} CP/MAS HETCOR 2D contour plot of Tsp-POSS/PS HPC.

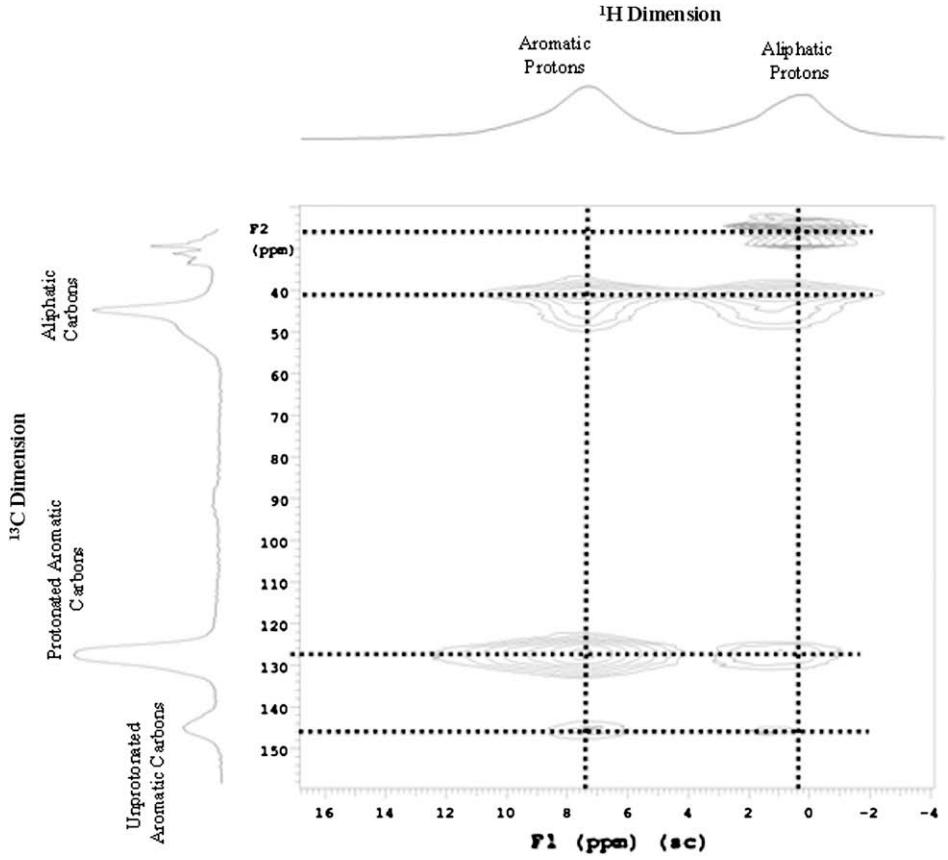

Fig. 12. $^{13}C\{^1H\}$ CP/MAS HETCOR 2D contour plot of Oib-POSS/PS HPC.

indicated by surface energy and bulk morphology analyses discussed in later sections. Differences in the dispersion and migration behavior are linked to the structural differences in the two types of POSS. The greater solubility of Tsp-POSS in PS, due to its phenyl substituents, allows greater POSS–PS intermolecular attractions and results in smaller and more uniform POSS domains. In Oib-POSS samples, on the other hand, POSS–PS interactions are weaker while POSS–POSS interactions are stronger, resulting in larger POSS aggregates.

TEM micrographs and corresponding EDAX elemental analysis of Tsp-POSS and Oib-POSS/PS blends are shown in Fig. 5(A) and (B), respectively. In the Tsp-POSS sample, small aggregates (5–10 nm) are observed distributed evenly through the bulk. The Oib-POSS sample shows large (>100 nm), widely dispersed aggregates. This behavior is consistent with the theoretical solubility predictions, and the enhanced Tsp-POSS dispersion is attributed to its higher compatibility with PS. EDAX elemental analysis of the aggregates indicates that they are POSS with the appearance of the signature peak of silicon at 1.75 KeV. The TEM studies also indicate that Oib-POSS preferentially migrates to the surface, while Tsp-POSS remains dispersed throughout the bulk.

WAXD diffraction studies were conducted to explore the crystalline structures of POSS in the PS matrix. X-ray diffractograms of POSS/PS HPCs and comparative diffractograms of neat PS, Oib-POSS and Tsp-POSS are shown in Fig. 6. Neat Oib-POSS exhibits characteristic crystalline peaks at $2\theta = 8.0°$, 8.9°, and 10.9°, whereas Tsp-POSS exhibits characteristic crystalline peaks at $2\theta = 7.2°$ and 8.7°. The presence of sharp peaks in the WAXD patterns of neat POSS samples indicates their highly crystalline nature. Neat PS exhibits two diffuse amorphous halos at $2\theta = 9.1°$ and 19.2°. The WAXD spectrum of the Oib-POSS/PS composite shows crystalline peaks corresponding to neat Oib-POSS and the amorphous halo of PS. The Tsp-POSS/PS HPC spectrum, on the other hand, appears very similar to that of neat PS, with no evident Tsp-POSS crystalline peaks. While the Oib-POSS aggregates maintain their highly crystalline structure when blended in the PS matrix, the nano-dispersed Tsp-POSS molecules show no apparent crystallinity.

Surface segregation of additives is often attributed to the drive to minimize overall surface energy. Surface energy measurements provide further indication of Oib-POSS surface segregation. Table 6 shows the surface energy of neat PS, POSS, and POSS/PS HPCs. Oib-POSS/PS films exhibit a surface energy value of 24 mN/m, similar to that of neat Oib-POSS, indicating significant surface segregation. Tsp-POSS/PS films, on the other hand, yield surface energy measurement of 35 mN/m, similar to that of neat PS (34 mN/m), indicating minimal surface segregation.

Assuming the surface energy of the composite is proportional to the fractional surface coverage of POSS (f_{POSS}), equation (1) can be used to estimate f_{POSS}. [54]

$$f_{POSS} = (\gamma_{composite} - \gamma_{PS})/(\gamma_{POSS} - \gamma_{PS}) \quad (1)$$

For Oib-POSS/PS composites, f_{POSS} is estimated at 78%, while Tsp-POSS/PS composites yield an estimate of 15% f_{POSS}. (Note that equation (1) is most appropriately applied to miscible blends. The values are provided only as a general comparison between the two systems.)

Thermodynamic driving forces for dispersion and segregation behavior of the POSS/PS blends can be examined using the Gibbs free energy of mixing (ΔG_m) equation (2), written in equation (3) for mixtures in terms of solubility parameters and volume fraction of each component.

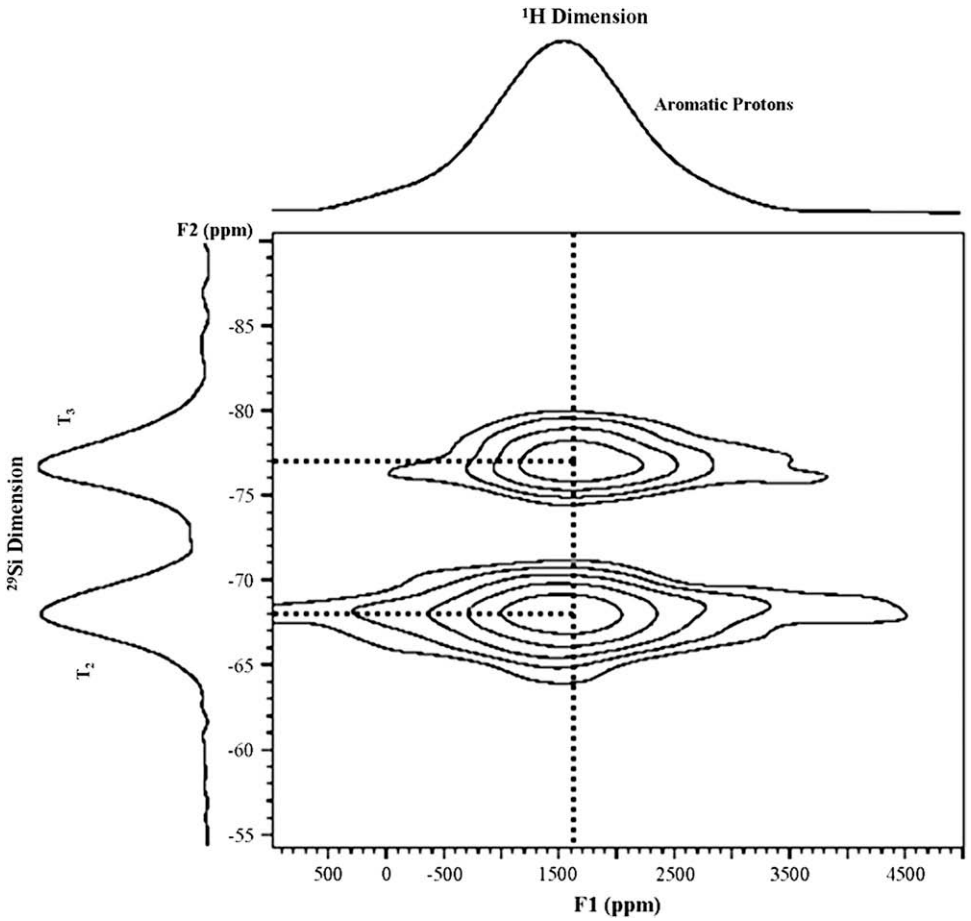

Fig. 13. $^{29}Si\{^{1}H\}$ CP/MAS HETCOR 2D contour plot of Tsp-POSS/PS HPC.

$$\Delta G_m = \Delta H_m - T\Delta S_m \quad (2)$$

$$\Delta G_m = V_1(\delta_1 - \delta_2)^2 \Phi_1 \Phi_2 + RT(n_1 \ln \Phi_1 + n_2 \ln \Phi_2) \quad (3)$$

where V = molar volume, δ = solubility parameter, Φ = volume fraction, n = mole fraction, R = gas constant, and T = absolute temperature.

Minimization of the positive enthalpy term (ΔH_m) and minimal decreases in entropy (ΔS_m) are necessary to achieve good mixing. If enthalpic interactions are substantially greater in magnitude than entropic interactions, the dispersion state is decided primarily by the difference in the solubility parameters. For Oib-POSS/PS blends, the relatively large difference in solubility parameters ($\Delta\delta_{\text{Oib-POSS/PS}} = 1.4\ (\text{cal/cm}^3)^{1/2}$) results in non-favorable enthalpic interactions that promote surface segregation of the POSS. In the Tsp-POSS case, the more favorable enthalpic interactions indicated by the similar solubility parameters ($\Delta\delta_{\text{Tsp-POSS/PS}} = 0.6\ (\text{cal/cm}^3)^{1/2}$) allow dispersion of Tsp-POSS throughout the bulk PS matrix.

If entropic forces dominate, the entropic penalty imposed by the presence of POSS particles on the mobility of the polymer chain becomes important. The size of POSS aggregates relative to the size of the polymer chains is critical. Theoretically, if the size of POSS aggregates is small compared to the radius of gyration (R_g) of the polymer chains, the entropic penalty for incorporating POSS into the polymer matrix should be small due to the minimal constraints placed on the conformation of the chains. In contrast, if the POSS aggregate size is large relative to R_g, the entropic penalty will be high due to the retardation of segmental motion of the polymer chains. In order to offset this high entropic penalty, individual polymer chains will extend and stretch away from POSS aggregates, driving surface segregation. Based on combined enthalpic and entropic considerations, it is therefore expected that in a PS matrix Tsp-POSS should disperse throughout the bulk, while Oib-POSS should segregate to the surface. Our TEM, AFM and surface energy results support this hypothesis.

Molecular miscibility and chain dynamics of the composites were analyzed through a series of solid-state NMR studies. Carbon CP/MAS spectra of open cage Tsp-POSS acquired with and without TOSS sequence are shown in Fig. 7(A) and (B), respectively. Sharp peaks are observed due to the crystalline nature of modified POSS. The four different NMR signals correspond to the phenyl carbons at the *para*- (a, 132 ppm), *meta*- (**b**, 128 ppm), and *ortho*- (**c**, 136 ppm) positions. The phenyl carbon attached to silicon oxide moiety on the POSS cage is labeled **d** (130 ppm). Carbon CP/MAS spectra of all samples are shown in Fig. 8(A)–(C). The PS spectrum exhibits resonances corresponding to the backbone methylene carbon **a** (39 ppm), the methine carbon **b** (42 ppm) attached to the phenyl ring, the quaternary aromatic carbon **c** (~145 ppm) and the aromatic carbons of phenyl ring at *ortho*-, *meta*-, and *para*-positions **d**, **e**, and **f** (120–137 ppm), respectively. The POSS/PS HPC spectrum shows signals corresponding to the aliphatic backbone carbon of the PS matrix as well as overlapping aromatic carbon peaks due to the presence of phenyl groups in both Tsp-POSS and PS. The small shoulders observed in the HPC spectra are probably due to the Tsp-POSS material. Although the low signal-to-noise ratio prevents any

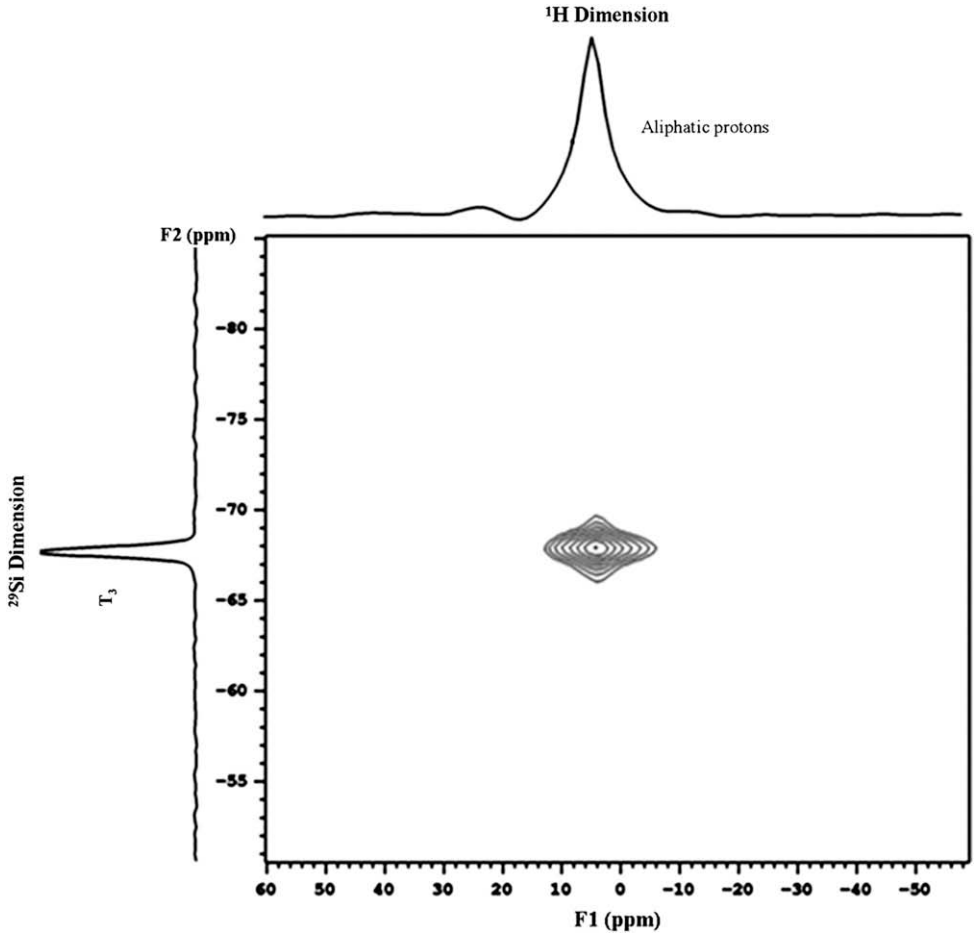

Fig. 14. $^{29}Si\{^{1}H\}$ CP/MAS HETCOR 2D contour plot of Oib-POSS/PS HPC.

extensive analysis, the broadness of the resonances suggests the modified POSS material is not in its original form, which in turn supports earlier data indicating its dispersion throughout the PS matrix.

Silicon CP/MAS NMR studies were implemented to obtain additional structural information regarding the interaction between Tsp-POSS and the PS matrix. The neat Tsp-POSS spectrum has sharp, narrow peaks between −64 and −72 ppm and −76 and −82 ppm, corresponding to T_2 and T_3 sites, respectively (Fig. 9A). Unmodified closed cage POSS, a T_8 structure, has resonances between −65 to −67 ppm; thus, the chemical shift values observed for Tsp-POSS, a T_7 structure, are consistent [55–57]. However, upon blending Tsp-POSS with the PS matrix the ^{29}Si spectra broaden considerably (Fig. 9B). This is attributed to Tsp-POSS losing its crystalline nature and instead becoming dispersed on a molecular scale *via* π–π interactions. This is confirmed by comparing the ^{29}Si spectra of Oib-POSS and its HPC (Fig. 10(A) and (B)). Both samples show only a single, sharp resonance at −66 ppm. This indicates that the crystalline nature of Oib-POSS remains unchanged when blended into the PS matrix, and thus the POSS is not dispersed at the nanoscopic level. These findings complement the WAXD results. This hypothesis was further verified by two dimensional heteronuclear correlation experiments (^{1}H–^{13}C and ^{1}H–^{29}Si 2D HETCOR).

In solid-state 2D heteronuclear correlation NMR experiments chemical shifts from dipole coupled species are separated into different frequency dimensions. Recent studies have successfully utilized this technique in elucidating phase structure and chemical interactions in polymer blends [58,59]. Figs. 11 and 12 show the 2D contour plot of the $^{13}C\{^{1}H\}$ HETCOR spectrum of Tsp-POSS/PS and Oib-POSS/PS HPCs respectively, with the ^{1}H projection and a separately acquired ^{13}C CP/MAS spectra plotted along the horizontal and vertical axis, respectively. The ^{1}H projection shows two broad proton resonances attributed to aromatic protons (downfield) and aliphatic protons (upfield). In Tsp-POSS/PS HPCs (Fig. 11) the aromatic and aliphatic carbons for PS are strongly correlated to both proton analogs. This is expected, since all the carbon and proton sites are in close proximity. In addition, however, there is a small but observable correlation between the downfield shoulder of the aromatic ring carbon and the aromatic ring proton, due to the phenyl groups of Tsp-POSS. In addition, the 2D plot for Oib-POSS/PS HPC (Fig. 12) shows the expected C–H correlations for PS and Oib-POSS. No crosspeaks are observed between Oib-POSS carbons and PS protons. This is consistent with the relatively poor compatibility and dispersion of Oib-POSS in PS.

The $^{29}Si\{^{1}H\}$ CP/MAS HETCOR 2D contour plot for Tsp-POSS/PS HPC is shown in Fig. 13, with a separate ^{29}Si CP/MAS spectrum and the ^{1}H projection shown along the vertical and horizontal axis, respectively. The contour plot clearly shows the two ^{29}Si peaks (T_2 and T_3) correlate only to the aromatic ^{1}H moiety. This supports Tsp-POSS being in close spatial proximity with nearby PS chains. Similar spectra were also acquired for Oib-POSS/PS HPCs (Fig. 14). The plot shows only a correlation between the isobutyl aliphatic protons (assignment based on the small width of the ^{1}H projection) with the T_3 silicon site. This indicates that Oib-POSS molecules are located spatially far from PS chains, and is in line with the light scattering observations discussed earlier.

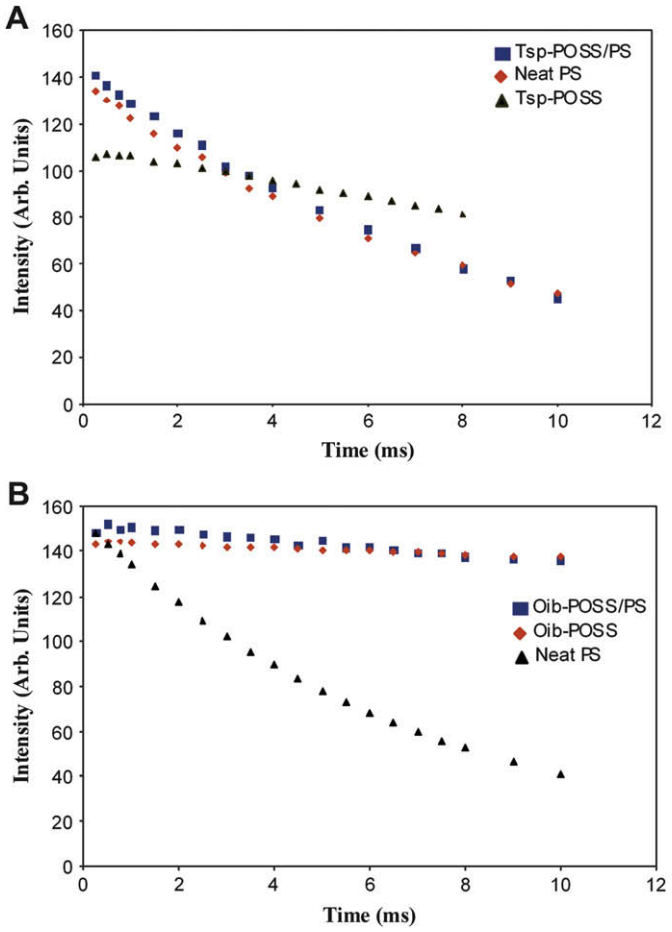

Fig. 15. $T_{1\rho}$(H) relaxation decay of (A) neat PS, Tsp-POSS, and Tsp-POSS/PS HPC and (B) neat PS, Oib-POSS, and Oib-POSS/PS HPC.

Furthermore, solid-state rotating-frame proton spin-lattice relaxation ($T_{1\rho}$ (H)) experiments, which are sensitive to the molecular motions occurring in the 10–100 kHz range, were performed to gain additional insight about the miscibility and homogeneity of POSS/PS HPCs. The numerical values of relaxation time constant are associated with the number of phases in a mixture, which in turn provides information about the miscibility and homogeneity in a multi-component polymer system at the nanometer scale. Fig. 15(A) shows the plot of ^{13}C resonance intensity versus spin-locking time for the protonated aromatic carbon for Tsp-POSS, neat PS, and the HPC. Within the experimental error, the $T_{1\rho}$ (H) relaxation decay of Tsp-POSS/PS HPCs follows a mono-exponential trend which mirrors the relaxation decay of neat PS. This contrasts the relaxation decay behavior of Tsp-POSS, which exhibits a slower decay rate typical for crystalline solids. This result indicates that for the Tsp-POSS/PS HPC a homogeneous distribution of Tsp-POSS exists within the polystyrene matrix. Fig. 15(B) shows the ^{1}H $T_{1\rho}$ data for the aliphatic protons of Oib-POSS and Oib-POSS/PS HPC, as well as the styrene methylene/methine protons of the Oib-POSS/PS HPC. Here the Oib-POSS sites have nearly identical relaxation behavior. If the POSS material had been dispersed throughout the PS matrix at a molecular level, the relaxation behavior would have mirrored the PS methylene decay. These observations suggest that Oib-POSS is not distributed homogeneously, but instead forms aggregates.

It should be noted that $T_{1\rho}$ (H) measurements are dominated by spin diffusion and provide information about the relaxation of the whole system rather than the dynamics of chain segments. In order to understand factors favoring the better miscibility in the Tsp-POSS/PS system, carbon rotating-frame spin-lattice relaxation times ($T_{1\rho}$ (C)) were measured. Carbon $T_{1\rho}$ relaxation is not influenced by spin diffusion, due to small ^{13}C–^{13}C dipolar coupling arising from the low natural abundance and large separation of the nuclei. It should be noted that the decay of ^{13}C magnetization under spin-locking conditions is the sum of ^{13}C $T_{1\rho}$ and cross-relaxation between carbons and protons (T^{D}_{1CH}). For carbons in semi-crystalline polymers, the T^{D}_{1CH} term dominates, whereas for carbons in glassy polymers the main term is ^{13}C $T_{1\rho}$ spin-lattice relaxation.

To understand the relaxation processes contributing to $T_{1\rho}$(C) and to probe the effect of POSS molecules on the chain dynamics of the PS matrix, $T_{1\rho}$(C) relaxation times of the aromatic region for the Tsp-POSS cage, aromatic region of the PS chain and backbone aliphatic region of PS were measured at various spin-locking fields. Here an exponential dependence on the RF spin-locking field indicates the domination of the cross-relaxation mechanism, while a quadratic dependence means molecular motion is dominant. Figs. 16 and 17 show the RF-dependence of the $T_{1\rho}$(C) relaxation times for the aromatic and aliphatic sites, respectively. There is no clear trend observed for the aromatic carbons for PS and Tsp-POSS, and the Oib-POSS/PS material shows little variation with RF spin-locking strength. The complexity in the relaxation behavior for the phenyl rings is probably due to the large chemical shift anisotropy of these moieties, which provide an additional relaxation mechanism. Fig. 17, however, clearly shows the presence of Tsp-POSS affects $T_{1\rho}$(C) relaxation times for the aliphatic carbon positions. This is expected, since the motional behavior of the polymer backbone would be affected by Tsp-POSS segregating close to the PS chains (*via* π–π interactions between

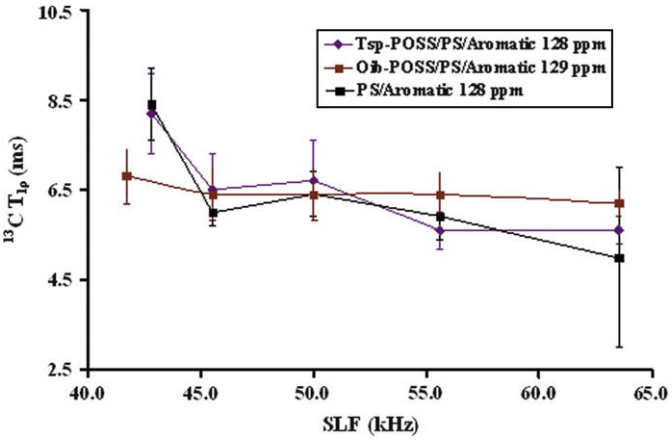

Fig. 16. Change in $T_{1\rho}$(C) relaxation time of aromatic region of PS, Tsp-POSS/PS, and Oib-POSS/PS HPCs as a function of spin-locking fields.

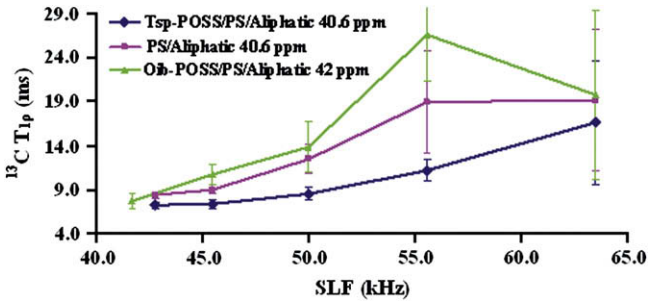

Fig. 17. Change in $T_{1\rho}$(C) relaxation times of aliphatic region of PS, Tsp-POSS/PS, and Oib-POSS/PS HPCs as a function of spin-locking fields.

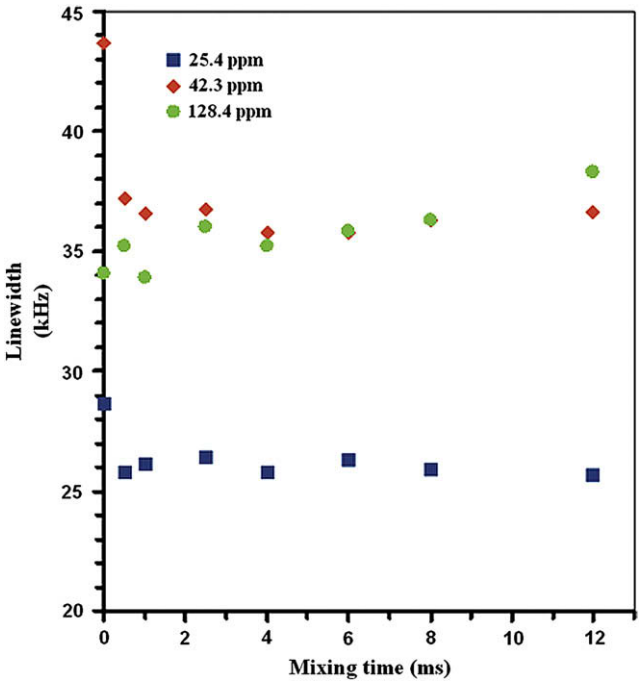

Fig. 18. Change in ^{1}H line-widths of Oib-POSS/PS HPC as a function of mixing time.

phenyl rings). The presence of Oib-POSS, while slightly increasing T_1(C) relaxation times, does not perturb the overall RF-field dependence. This behavior is consistent with Oib-POSS acting simply as a filler material.

The ^{1}H line-shape can also be used to investigate the molecular dynamics of polymers. However, line-widths are difficult to measure directly from the spectrum due to the low ^{1}H resolution as compared to the chemical shift. The WISE experiment is a pertinent tool to measure the dipolar line-widths in which carbon chemical shifts appear in the detected (F_2) dimension and its corresponding proton line-width appears in the indirect (F_1) dimension. Information about the molecular dynamics and miscibility of polymer blends is obtained from this method. For miscible polymer blends, the ^{1}H line-width will become equal for all carbon sites as the mixing time is increased *via* spin diffusion, while in immiscible systems this will not occur. Fig. 18 shows the change of proton line-widths versus various mixing times for the aromatic and aliphatic regions of Oib-POSS/PS. No significant change in proton line-widths was observed with increasing mixing time, indicating lack of interaction and immiscibility between Oib-POSS and the PS matrix in all regions.

4. Conclusions

These studies show that POSS solubility and dispersion in a polystyrene matrix can be tailored by varying the substituent organic groups. Calculated solubility parameter proved to be a useful tool for predicting dispersion and segregation of POSS molecules in the polystyrene matrix, and should be applicable to other POSS/polymer systems. Solution and solid-state studies demonstrated POSS/polymer chain interactions and their relationship to POSS structure and chemical composition. The results from these studies help to explain surface modification behavior observed in these and previous reports of POSS/polymer composites prepared *via* melt and solution processes, and suggest possibilities for tailoring surface and bulk properties of POSS/polymer nanocomposites through control of the POSS structure. Surface modification of thin films through control of nanostructure is of particular interest for applications such as micro/nanoelectronics and biomedical devices where the ability to alter surface energy and enhance hardness, modulus and tribological properties is important. Maintaining transparency in such films through nano-dispersion enables further opportunities. Bulk modification through molecular level dispersion of POSS enables synergistic enhancement of thermomechanical properties of composites and nanocomposites.

In the solution and solid-state studies performed, Tsp-POSS, with similar solubility parameter to that of PS, consistently demonstrated enhanced dispersion and miscibility with the PS matrix in comparison to Oib-POSS/PS blends, which posses a significantly larger solubility parameter difference. Solution dynamics, investigated *via* dynamic and multiangle laser-light scattering, indicated enhanced interaction between PS chains and Tsp-POSS, while Oib-POSS/PS solutions showed Oib-POSS aggregates and limited POSS/PS interaction. Films produced from the solutions were transparent for Tsp-POSS blends but hazy for Oib-POSS blends. Microscopy (AFM/TEM) and surface energy measurements indicated miscible Tsp-POSS/PS blends with nano-level Tsp-POSS dispersion, while Oib-POSS blends demonstrated preferential surface segregation and Oib-POSS aggregation. Surface segregation of Oib-POSS is attributed to the non-favorable enthalpic interactions and high entropic penalty imposed on PS chains through incorporation of large POSS aggregates.

WAXD and solid-state NMR studies demonstrated that Tsp-POSS molecules lose crystallinity on incorporation in the PS matrix, while Oib-POSS crystallinity levels remain constant. Silicon CP/MAS NMR spectra of neat Tsp-POSS exhibit sharp peaks attributed to the crystalline nature of POSS. Similar spectra of Tsp-POSS/PS blends show two broad peaks, indicating reduction in crystallinity and suggesting that Tsp-POSS disperses on a molecular level when blended with PS. Furthermore, 2D HETCOR studies show strong correlation between the two Si peaks of Tsp-POSS (T_2 and T_3) with the aromatic proton from PS. This is attributed to the close spatial proximity of Tsp-POSS molecules and PS chains driven by π–π attractions between the phenyl rings. In contrast, Oib-POSS/PS samples exhibit weak resonance correlation between the silicon peak from POSS and the aliphatic protons from PS. Significant differences in the relaxation behavior for the blends were observed in proton spin-lattice relaxation studies. Neat PS and Tsp-POSS/PS blends exhibit overlapping mono-exponential decay behavior, indicating molecular level dispersion of Tsp-POSS. Entirely different decay curves were obtained for Oib-POSS/PS blends, indicating inhomogeneity in Oib-POSS dispersion. Furthermore, proton line-widths measurements at various mixing times (WISE studies), indicate lack of interaction and immiscibility of Oib-POSS with PS.

Acknowledgements

This work was supported primarily by the Office of Naval Research, award no. N00014-07-1-1057. The authors would like to acknowledge Hybrid Plastics Inc., MS for providing POSS materials. The authors would also like to thank Dr. Christopher Rulison (Augustine Scientific Inc., OH) and Adam Smith (McCormick research group, USM) for their help in surface energy and light scattering measurements, respectively.

References

[1] Chen GX, Shimizu H. Polymer 2008;49:943–51.
[2] Wheeler PA, Misra R, Cook B, Morgan SE, Lichtenhan JD. J Appl Polym Sci 2008;108:2503–8.

[3] Lichtenhan JD, Schwab JJ, Reinerth WA. Chem Innovation 2001;31:3–5.
[4] Lichtenhan JD. Comments Inorg Chem 1995;17:115–7.
[5] Shockey EG, Bolf AG, Jones PF, Schwab JJ, Chaffee KP, Haddad TS, et al. Appl Organomet Chem 1999;13:311–27.
[6] Lee A, Lichtenhan JD. J Appl Polym Sci 1999;73:1993–2001.
[7] Romo-Uribe A, Mather PT, Haddad TS, Lichtenhan JD. J Polym Sci Part B Polym Phys 1998;36:1857–72.
[8] Patel RR, Mohanraj R, Pittman CU. J Polym Sci Part B Polym Phys 2006;44: 234–48.
[9] Lee A, Lichtenhan JD. Macromolecules 1998;31:4970–4.
[10] Turri S, Levi M. Macromolecules 2005;38:5569–74.
[11] Mather PT, Jeon HG, Romo-Uribe A, Haddad TS, Lichtenhan JD. Macromolecules 1999;32:1194–203.
[12] Fu BX, Hsiao BS, Pagola S, Stephens P, White H, Rafailovich M, et al. Polymer 2001;42:599–611.
[13] Zhao Y, Schiraldi DA. Polymer 2005;46:11640–7.
[14] Fina A, Tabuani D, Frache A, Camino G. Polymer 2005;46:7855–66.
[15] Ning H, Martin B, Andreas S. Macromolecules 2007;40:9672–9.
[16] Hosaka N, Torikai N, Otsuka H, Takahara A. Langmuir 2007;23:902–7.
[17] Kidane AG, Edirisinghe MJ, Bonhoeffer P, Seifalian AM. Biorheology 2007;44:265–72.
[18] Funke W. J Oil Colour Chem Assoc 1976;59:398–400.
[19] Eisenriegler E, Kremer K, Binder K. J Chem Phys 1982;77:6296–9.
[20] Ober R, Paz L, Taupin C, Pincus P, Boileau S. Macromolecules 1983;16:50–2.
[21] Shull KR, Kramer EJ, Hadziioannou G, Tang W. Macromolecules 1990;23: 4780–2.
[22] Leibler L. Makromol Chem Macromol Symp 1988;16:1–2.
[23] Gaines GL. J Phys Chem 1969;73:3143–5.
[24] Misra R, Fu BX, Morgan SE. J Polym Sci Part B Polym Phys 2007;45:2441–55.
[25] Misra R, Fu BX, Plagge A, Morgan SE. J Polym Sci Part B Polym Phys, in press.
[26] Hosaka N, Otsuka H, Hino M, Takahara A. Langmuir 2008;24:5766–72.
[27] Paul R, Karabiyik U, Swift MC, Esker AR. Langmuir 2008;24:5070–9.
[28] Paul R, Karabiyik U, Swift MC, Hottle JR, Esker AR. Langmuir 2008;24:4676–84.
[29] Koh K, Sugiyam S, Morinaga T, Ohno K, Tsuji Y, Fukuda T, et al. Macromolecules 2005;38:1264–70.
[30] Gupta S, Zhang Q, Emrick T, Balazs AC, Russell TP. Nat Mater 2006;5:229–32.
[31] Mackay ME, Tuteja A, Duxbury PM, Hawker CJ, Horn BV, Guan Z, et al. Science 2006;311:1740–3.
[32] Krishnan RS, Mackay ME, Duxbury PM, Pastor A, Hawker CJ, Horn BV, et al. Nano Lett 2007;7:484–9.
[33] Stejskal EO, Schaefer J, Sefcik MD, McKay RA. Macromolecules 1981;14:275–8.
[34] Clauss J, Schimidt-Rohr K, Adam A, Boeffel C, Spiess HW. Macromolecules 1992;25:5208–11.
[35] Hou SS, Bonagamba TJ, Beyer FL, Madison PH, Schmidt-Rohr K. Macromolecules 2003;36:2769–72.
[36] Brus J, Urbanova M, Strachota A. Macromolecules 2008;41:372–86.
[37] Washburn EW. Phys Rev 1921;17:374–6.
[38] Fowkes FM, Kaczinski MB, Dwight DW. Langmuir 1991;7:2464–70.
[39] Owens DK, Wendt RC. J Appl Polym Sci 1969;13:1741–7.
[40] Schaefer J, Stejskal EO, Buchdahl R. Macromolecules 1977;10:384–7.
[41] Dixon WT. J Chem Phys 1982;77:1800–9.
[42] Bielecki A, Kolbert AC, Levitt MH. Chem Phys Lett 1989;155:341–6.
[43] Clauss J, Schmidt-Rohr K, Spiess HW. Acta Polymer 1993;44:1–4.
[44] Schmidt-Rohr K, Clauss J. Macromolecules 1992;25:3273–6.
[45] Hoy KL. J Paint Technology 1970;42:76–118.
[46] Hoy KL. Group molar-attraction constants. In: Bradrup J, Immergut EH, editors. Polymer handbook. 2nd ed. New York: Wiley & Sons; 1975. p. IV-339.
[47] Liu L, Ming T, Liang G, Chen W, Zhang L, Mark JE. J Macromol Sci Part A Pure Appl Chem 2007;44:659–64.
[48] Pusey PN, Vaughan JM, Williams VG. J Chem Soc Faraday Trans 1974;70: 1696–700.
[49] Braun B, Dorgan JR, Chandler JP. Biomacromolecules 2008;9:1255–63.
[50] Mays JM, Terao K. Eur Polym J 2004;40:1623–7.
[51] Negadi A, Duval M, Benmouna M. Polym Bull 1999;43:261–7.
[52] Burchard W, Schmidt M, Stockmayer WH. Macromolecules 1980;13:580–7.
[53] Akcasu ZA, Benmouna M. Macromolecules 1978;11:1193–6.
[54] Bhatia QS, Pan DH, Koberstein JT. Macromolecules 1988;21:2166–75.
[55] Unno M, Alias SB, Saito H, Matsumoto H. Organometallics 1996;15:2413–5.
[56] Feher FJ, Souvilong D, Lewis GT. J Am Chem Soc 1997;119:11323–6.
[57] Rikowski E, Marsmann HC. Polyhedron 1997;16:3357–9.
[58] Li S, Rice DM, Karasz FE. Macromolecules 1994;27:2211–5.
[59] White JL, Mirau PA. Macromolecules 1994;27:1648–50.